Strain engineering magnetocrystalline anisotropy in strongly correlated VTe$_2$ with room-temperature ferromagnetism

Zhiyuan Tang, Yancong Chen, Yue Zheng, and Xin Luo [*]

Guangdong Provincial Key Laboratory of Magnetoelectric Physics and Devices, School of Physics, Sun Yat-sen University, Guangzhou 510275, China;
State Key Laboratory of Optoelectronic Materials and Technologies, School of Physics, Sun Yat-sen University, Guangzhou 510275, China;
and Centre for Physical Mechanics and Biophysics, School of Physics, Sun Yat-sen University, Guangzhou 510275, China

Two-dimensional (2D) magnetic transition metal dichalcogenides have attracted great interest in various fields, including information storage, logic devices, and high-frequency detectors. However, the currently reported 2D magnets are limited by their low Curie temperatures. Based on the density-functional theory calculation, we predicted the metastable H phase VTe$_2$ (H-VTe$_2$) is a promising room-temperature 2D in-plane ferromagnetic semiconductor without charge-density wave (CDW) transition. To achieve the H-VTe$_2$ from the T phase or CDW-phase VTe$_2$, electron doping is proposed as a feasible strategy in practice. Moreover, the significant modulation effect of external strain fields on the magnetocrystalline anisotropy energy and magnetic ordering of monolayer H-VTe$_2$ are systematically studied. The electron correlation included from a Hubbard-U term has a profound influence on the ground state of magnetic order of H-VTe$_2$, as well as the direction of the easy-magnetization axis. These results not only provide an in-depth understanding of the modulation mechanism of the magnetic H-VTe$_2$, but also shed light on the potential applications of H-VTe$_2$ in spintronics and sensors.

I. INTRODUCTION

Two-dimensional (2D) transition metal dichalcogenides (TMDs) MX_2 (M = transition-metal; X = S, Se, Te) [1,2] have been attracting great attention for their remarkable physical properties ranging from ferromagnetism [3], superconductivity [4], quantum Hall effect [5,6], Mott insulators [7] to charge-density wave [8,9], etc. In addition, TMDs can be combined to construct heterostructures easily due to their weak interlayer van der Waals interactions [10]. The TMDs have great potential in low-dimensional spintronic devices, which mainly use the intrinsic ferromagnetism (FM) and spin-orbit coupling(SOC) of the TMDs [11]. Recently, several 2D magnets such as CrX_3 (X = I, Br, Cl) [12–14], Fe$_3$GeTe$_2$ [15], etc., were successfully demonstrated experimentally and had been used to construct spintronic devices, e.g., spin tunnel field-effect transistor [16], spin-filter magnetic tunnel junction [17], and tunneling spin valve [18]. However, they are limited by the low Curie temperature (45 K and 68 K for monolayer CrI$_3$ [12] and Fe$_3$GeTe$_2$ [15], respectively) and structural instability at monolayer thickness. Recent reports have uncovered that some TMDs are ferromagnetic with higher Curie temperature and better stability [19,20]. In particular, the monolayer H-phase vanadium dichalcogenides are predicted to be promising candidates for room temperature 2D magnets [21,22], with a strong SOC effect and valley polarization due to the broken-inversion symmetry [23,24]. Density-functional (DFT) calculations also found that the Coulomb interaction strongly affects the relative formation energy and stability

between H-phase and T-phase VSe$_2$ [25]. Experimentally, the VX_2 (X = S, Se, Te) synthesized with chemical vapor deposition or molecular-beam epitaxy method [26–28] are in T phase instead of H phase based on the scanning tunneling microscopy (STM) and low-energy electron diffraction measurement. The pristine ferromagnetic order was absent in monolayer T-VX_2 as reflected from x-ray magnetic circular dichroism and angle-resolved photoemission spectroscopy (ARPES) [9,29]. Recent work revealed that monolayer T-VX_2 may undergo a charge-density wave (CDW) phase transition originating from the electroacoustic coupling. The CDW transition was found to reduce the electronic density at the Fermi surface and inhibit ferromagnetic order [30]. Detailed STM results indicated that the CDW transition of T-VTe$_2$ had a $4 \times 4 \times 1$ supercell lattice and atomic distortion with the critical temperature of 186 K [31,32]. These results were further confirmed by ARPES measurement that the d bands near the Fermi surface have partial band-gap opening, which weakened the magnetism-related electron coupling [32]. In light of this, it seems paramount to unveil the deeper mechanism related to the ground state of the VTe$_2$. Most importantly, how to modulate the magnetic H-VTe$_2$ state in practice is another important issue.

Motivated by the above questions, in this work, we carried out first-principles calculations to explore the connection between the structures and magnetic properties of VTe$_2$ monolayer. We found that the structural instability of T-VTe$_2$ defines the CDW ground state at low temperature, which inhibits the ferromagnetic phase. By considering the electron correlation, the CDW-phase VTe$_2$ is the ground state at low temperature, while the T phase and H phase will become favorable in turn at the higher temperature. Moreover, the

*luox77@mail.sysu.edu.cn

magnetic H-VTe$_2$ could become the ground state with moderate electron doping or strain engineering at low temperature, for example, using the 11% Mn or 5.6% S doping. The H-VTe$_2$ is predicted to have intrinsic ferromagnetism (FM) without any CDW transition based on its phonon dispersion. In addition to solving the realization of the interesting magnetic ground state of VTe$_2$, these results have broad impacts on the 2D semiconducting magnetic H-VTe$_2$, including the effective modulation of magnetism and its applications in spintronics.

II. METHODS

Our first-principles calculations were based on DFT as implemented in the Vienna *Ab initio* Simulation Package (VASP) [33,34]. The generalized gradient approximation in the parametrization of Perdew-Burke-Ernzerhof (PBE) was chosen as the exchange and correction functional [35]. The Heyd-Scuseria-Ernzerhof hybrid functional (HSE06) [36], with the inclusion of SOC effect [37], was also used to obtain an accurate band structure. A plane-wave basis with an energy cutoff of 500eV was used during the structural relaxations. The electron states of $3s^2 3p^6 3d^3 4s^2$ in V and $5s^2 5p^4$ in Te were treated as valence states. To avoid the interlayer interaction, a vacuum layer of 16 Å along the c axis was added to the slabs. The search of ground-state structures of VTe$_2$ was done with the structure prediction program CALYPSO [38] based on the particle-swarm optimization algorithm. On-site Coulomb interaction to the V $3d$ orbitals (PBE + U) [39] was self-consistently calculated based on the constrained random-phase approximation [40]. The value of Coulomb repulsion U and exchange interaction J were adopted as 1.809 and 0.041 eV, 1.798 and 0.038 eV, and 1.976 and 0.034 eV for H-VTe$_2$, T-VTe$_2$, and T'-VTe$_2$, respectively. The Brillouin zone was sampled by using the converged k-point meshes, and the Gamma-centered $18 \times 18 \times 1$ and $4 \times 4 \times 1$ meshes are used for primitive unit cell and $4 \times 4 \times 1$ supercell of CDW phase, respectively. During the structure relaxation, the convergence criteria for maximum forces and energy differences were, respectively, set to 0.01 eV/Å and 10^{-5} eV. The *ab initio* molecular-dynamics (AIMD) simulation [41] with Andersen thermostat [42] for canonical ensemble (NVT) was performed at 300 K with the time step of 5 fs to test the thermal stability of H-VTe$_2$. The total simulation time for the $4 \times 4 \times 1$ supercell of monolayer H-VTe$_2$ was set to 10 ps. The structure stability was evaluated via phonon dispersion calculated using the $4 \times 4 \times 1$ supercell in the PHONOPY package [43]. The Helmholtz free energy is calculated by $F = E_{DFT} + E_{ZPE} - TS(\upsilon)$, where E_{DFT}, E_{ZPE}, and $TS(\upsilon)$, respectively, represent the DFT-calculated energy, zero-point energy (ZPE), and vibrational entropic contribution.

III. RESULTS AND DISCUSSION

A. Different phases of VTe$_2$

Based on the Genetic Algorithm structural searching results, we found that the T phase (D_{3d}), T' phase (C_{2h}), and H phase (D_{3h}) are the three lowest-energy candidates for the ground states of VTe$_2$ (Table SI and Fig. S1 in the Supplemental Material [44]). Since the T'VTe$_2$ origi-

nates from T-VTe$_2$ by lattice distortion [45], we focus on the T- and H-phase VTe$_2$ shown in Figs. 1(a) and 1(b). The calculated lattice constants of T- and H-phase VTe$_2$ are 3.68 and 3.64 Å, respectively, consistent with the experimentally measured lattice constants of T-VTe$_2$ [46,47]. To test the structural stability, we started with the phonon dispersion of both phases. The dispersion of high-symmetry T-VTe$_2$ in Fig. 1(c) reveals several structural instabilities, implying potential phase transitions at low temperature. The distortion associated with the imaginary frequencies at M point leads to T'-VTe$_2$, where the V atoms are dimerized to form a zigzag chain [Fig. S1(b)], while the soft mode of the second-lowest branch along the K-Γ in reciprocal space indicates another structural instability, which may freeze and generate a superstructure at low temperature. Instructed by the second soft mode, we constructed the star configuration in $4 \times 4 \times 1$ supercell [Fig. 1(e)] and hexagon configuration in $2\sqrt{3} \times 2\sqrt{3} \times 1$ supercell [Fig. 1(f)]. The optimized superstructures are stable and consistent with the recent experimental observed CDW phases of T-VTe$_2$ below the 186 K [28,29], which are well known to compete with the magnetic order [9,29,30]. We used the Stoner itinerant model to analyze the magnetic properties as both T- and CDW phases show metallicity [48,49] (Fig. S2). The Stoner criterion $IN(E_F) > 1$ gives the ferromagnetism in metallic systems, where $N(E_F)$ is the density of state (DOS) at Fermi energy (E_F) and Stoner parameter I is related to the average splitting energy $\langle \varepsilon_s \rangle$ and magnetic moments $\langle M \rangle$ for V atoms. The calculated $IN(E_F)$ is 0.88 and 0.53 for T-phase and CDW-phase VTe$_2$, respectively. The formation of CDW phase would further suppress the magnetism of T-VTe$_2$.

As shown in Table I and Fig. S5, the H-VTe$_2$ has slightly higher energy when considering the on-site Coulomb interactions. The star CDW phase (C_{3i}) has the lowest energy at zero temperature, which agrees with the experimental observation, i.e., CDW phase appears below the critical temperature, while $T(')$ phase is observed at room temperature [45]. However, there is no imaginary frequency in the phonon dispersion of H-VTe$_2$ [Fig. 1(d)], suggesting no CDW transition in H-VTe$_2$ (also proved in Fig. S3). Its elastic stiffness constants satisfy the well-known Born stability criteria [50], confirming the mechanical thermal stability of H-VTe$_2$ (Table SII). We also performed the dynamic AIMD (Fig. S4) simulations under the temperature of 300 K for 10 ps to test the thermal stability; no structural reconstructions happen from the total energy and snapshots of geometric structures. As shown in Fig. 1(h), the HSE06-calculated monolayer H-VTe$_2$ is a semiconducting magnetic TMDs with an indirect band gap of 0.457 eV (summarized in Table SIII).

Figure 2(a) suggests that the H-VTe$_2$ could become energy favorable above 625 K with the quasiharmonic vibrational free-energy correction. Strain engineering and carrier doping are widely used to induce the phase transition. By comparing the energy difference between T- and H-phase VTe$_2$ under external in-plane biaxial strain, electrostatic field, carrier doping, and out-of-plane strain in Fig. 2(b), Fig. 2(c), and Fig. S6, we found that electron doping is an effective way to achieve H phase with a critical carrier concentration of 8.52×10^{13} cm^{-2}, which can be achieved by interlayer charge transfer [51,52], intercalation [53,54], ionic liquid gating [55],
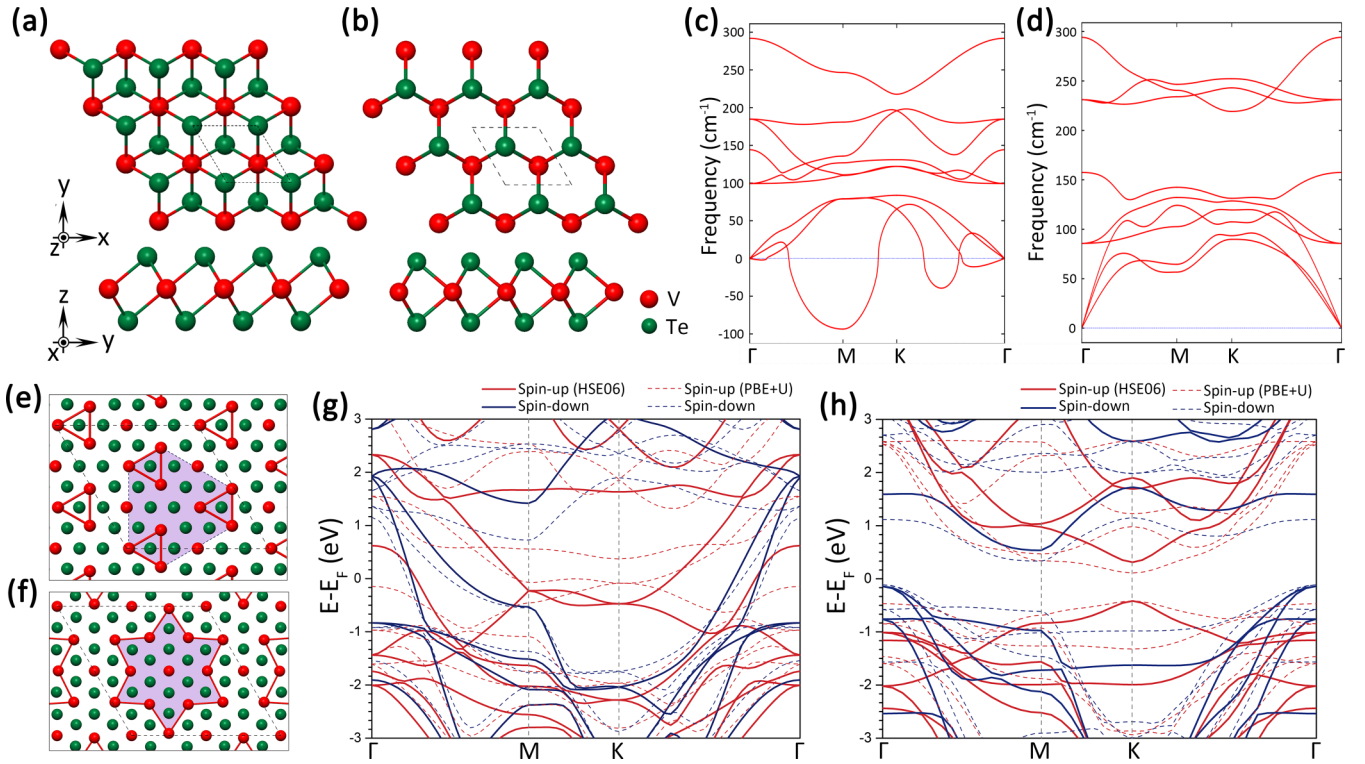
FIG. 1. Atomic structures of (a) T-VTe$_2$ and (b) H-VTe$_2$; the upper and down panels refers to the top view and side view, respectively. Phonon spectra of (c) T-VTe$_2$ and (d) H-VTe$_2$. The atomic structure of (e) triangle CDW phase and (f) star CDW phase constructed from the soft modes of T-VTe$_2$. Spin-polarized band structure of (g) T-VTe$_2$ and (h) H-VTe$_2$, both PBE+U (dot lines) and HSE06 (solid lines) functionals are used.

or atomic doping [56]. From the Bader charge analysis (Table SIV), the V atoms have higher valence states in H-VTe$_2$ due to the stronger electron transfer between V and Te atoms. The electron localization function analysis (Fig. S7) further supports that the electrons are strongly localized around Te and delocalized around V [57,58]. Since the valence states near Fermi energy are mainly contributed by the d orbitals of V for both H-VTe$_2$ and T-VTe$_2$ (Fig. S8), the doped electrons are likely to fill the d orbitals of V, the higher valence state in H-VTe$_2$ making it energy favorable under moderate electron doping. In addition, it is found that hole doping may further suppress the formation of CDW transition in T-VTe$_2$ (Fig. S9), which is proved in the T-VSe$_2$ in a recent work [59]. To have effective electron doping, dielectric gating and N-type atomic doping are widely used in the semiconductor community. Figure 2(d) shows that the H-VTe$_2$ becomes ground state in 11% Mn and 5.6% S doping. Finally, the climbing

image nudged elastic-band calculations indicate that there is an energy barrier of 0.582 eV to overcome when transforming from T phase to H phase without an external field [60] (Fig. S11). So, an annealing procedure is needed to get the stable H-VTe$_2$ from the experimental synthesis T-VTe$_2$ [61].

B. The magnetic properties of H-VTe$_2$.

After addressing the stability and availability of H-phase VTe$_2$, we focus on its magnetic properties. The total Hamiltonian to describe magnetic properties of semiconductor H-VTe$_2$ is described as

$$H = H_{\mathrm{MCA}} + H_{\mathrm{ex}}, \tag{1}$$

where H_{MCA} and H_{ex} represent the Hamiltonian of magnetocrystalline anisotropy (MCA) and exchange interaction between local magnetic moment, respectively.

H-VTe$_2$ belongs to the D_{3h} point group, so the d orbitals of V atoms can split into three groups, i.e., $E_1(dxy, dx^2\text{-}y^2)$, $E_2(dxz, dyz)$, and $A_1(dz^2)$. Figure 3(a) reveals the DOS of E_1, E_2, and A_1, which can be simplified to the energy diagram shown in Fig. 3(b). The exchange energy (0.3 eV) between spin up and spin down is small compared to the splitting energy (0.8 eV) of the crystal field, resulting in the low-spin state ($S = 1/2$, $M_S = 1.0\mu_B$) [62]. From the real-space net spin-density distributions in Fig. 3(c), we found that the localized magnetic moment of V atoms is mainly contributed by dz^2 orbital. The resulting in-plane (IP) isotropy and out-of-plane (OOP) anisotropy of VTe$_2$ magnetism can be
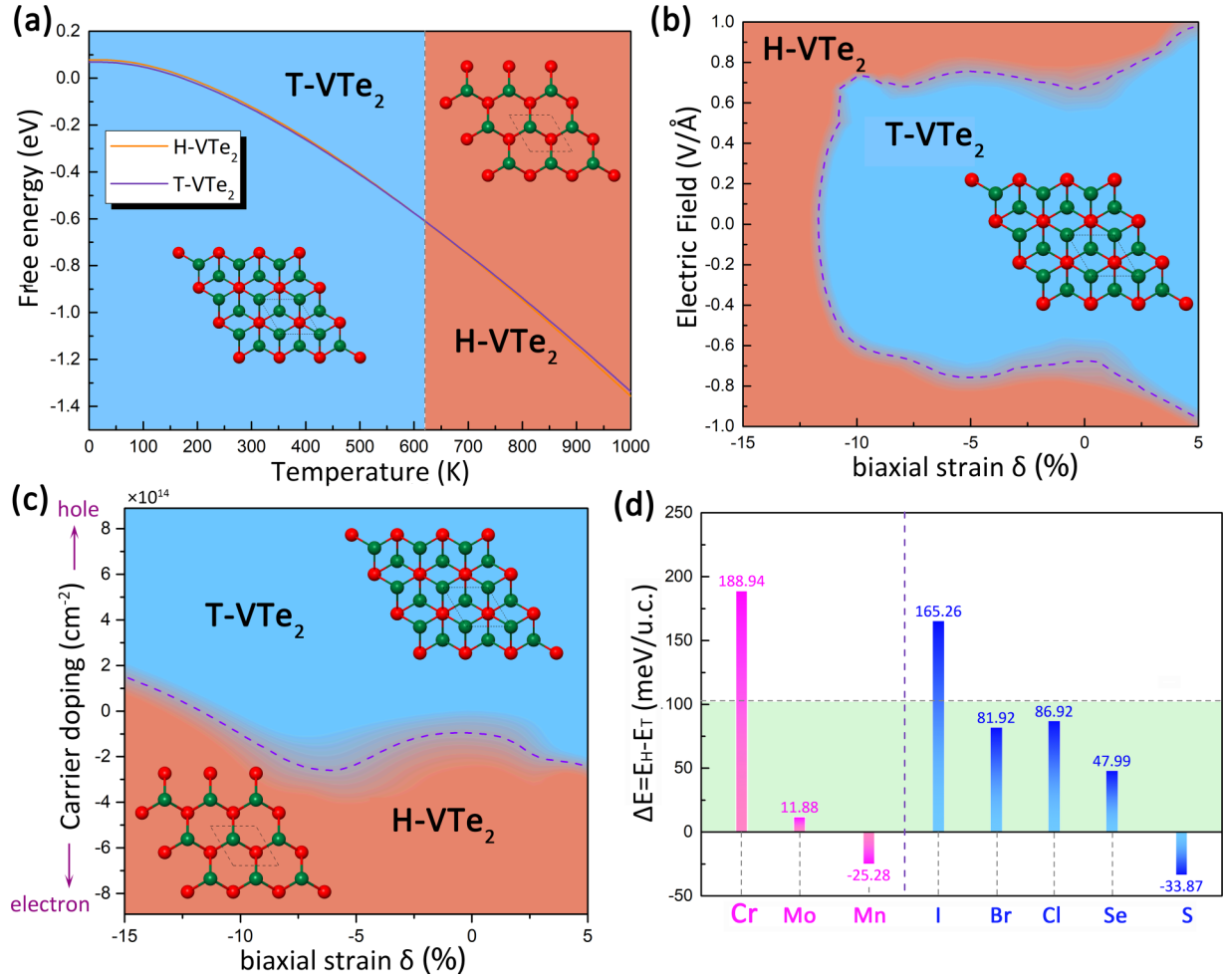
TABLE I. Calculated free energies of various phases of VTe$_2$ with and without Coulomb interaction; the energy of H-VTe$_2$ is set as reference.

	PBE (meV)	PBE + U (meV)
T phase	5.727	−103.000
T' phase	58.296	−20.261
H phase	0.000	0.000
Star-CDW	−19.613	−117.273

FIG. 2. (a) The Helmholtz free energies of the various VTe_2 phase as a function of temperature. (b) The VTe_2 phase diagram under biaxial strain and electrostatic field. (c) VTe_2 phase diagram under carrier doping and biaxial strain. (d) The energy difference between T-VTe_2 and H-VTe_2 with various doped atoms. The green area refers to the ΔE between nondoped T-VTe_2 and H-VTe_2.

described by H_{MCA}:

$$H_{MCA} = -\sum_i A_{zz} S_{i,z}^2,$$ (2)

where S_i and A_{zz}, respectively, represent the spin state and MCA coefficient at the ith site. The MCA originated from the SOC can be expressed as $\xi L \cdot S$ [63], where S is Pauli operator for spin and L is orbital angular momentum operator; ξ is the SOC constant. The magnetocrystalline anisotropy energy (MAE) is defined as the energy difference between the magnetic moment aligned in a specific direction and [001] direction. MAE is obtained by second-order perturbation theory [64,65]:

$$MAE = \frac{\xi^2}{4} \sum_{occ,unocc} \frac{|\langle \psi_{occ}|L_z|\psi_{unocc}\rangle|^2 - |\langle \psi_{occ}|L|\psi_{unocc}\rangle|^2}{E_{unocc} - E_{occ}},$$ (3)

where ψ_{occ} and ψ_{unocc} refer to the occupied and unoccupied wave functions without perturbation, respectively, and E_{occ} and E_{unocc} are the corresponding energy.

From the calculated MAE, the easy plane of H-VTe_2 is within the XY plane where the magnetization is isotropic as shown in Fig. 3(d) and Fig. S12. In addition, the value of Coulomb repulsion U and exchange interaction J can change the exchange splitting of d orbitals and the overlap of orbitals, thus influencing the magnitude of MAE and the direction of the easy-magnetization axis [66,67]. The Coulomb repulsion and exchange interaction favors the OOP and IP MAE, respectively, which can be modulated by the external biaxial strain but not carrier doping (Figs. S13 and S14). By increasing the tensile biaxial strain, the critical Coulomb repulsion U_c responsible for IP to OOP MCA transition is decreasing (Fig. S13). Therefore, we can realize the OOP easy-magnetization axis in H-VTe_2 with a 4% tensile biaxial strain, as revealed in Fig. 3(e). Additionally, the isotropic IP MCA can be broken under the in-plane uniaxial strain [Fig. 3(f)], with the easy-magnetization axis perpendicular to the compressive direction.

On the other hand, the exchange interaction between magnetic V atoms determines the overall magnetic ordering. To understand the mechanism of exchange interaction, the
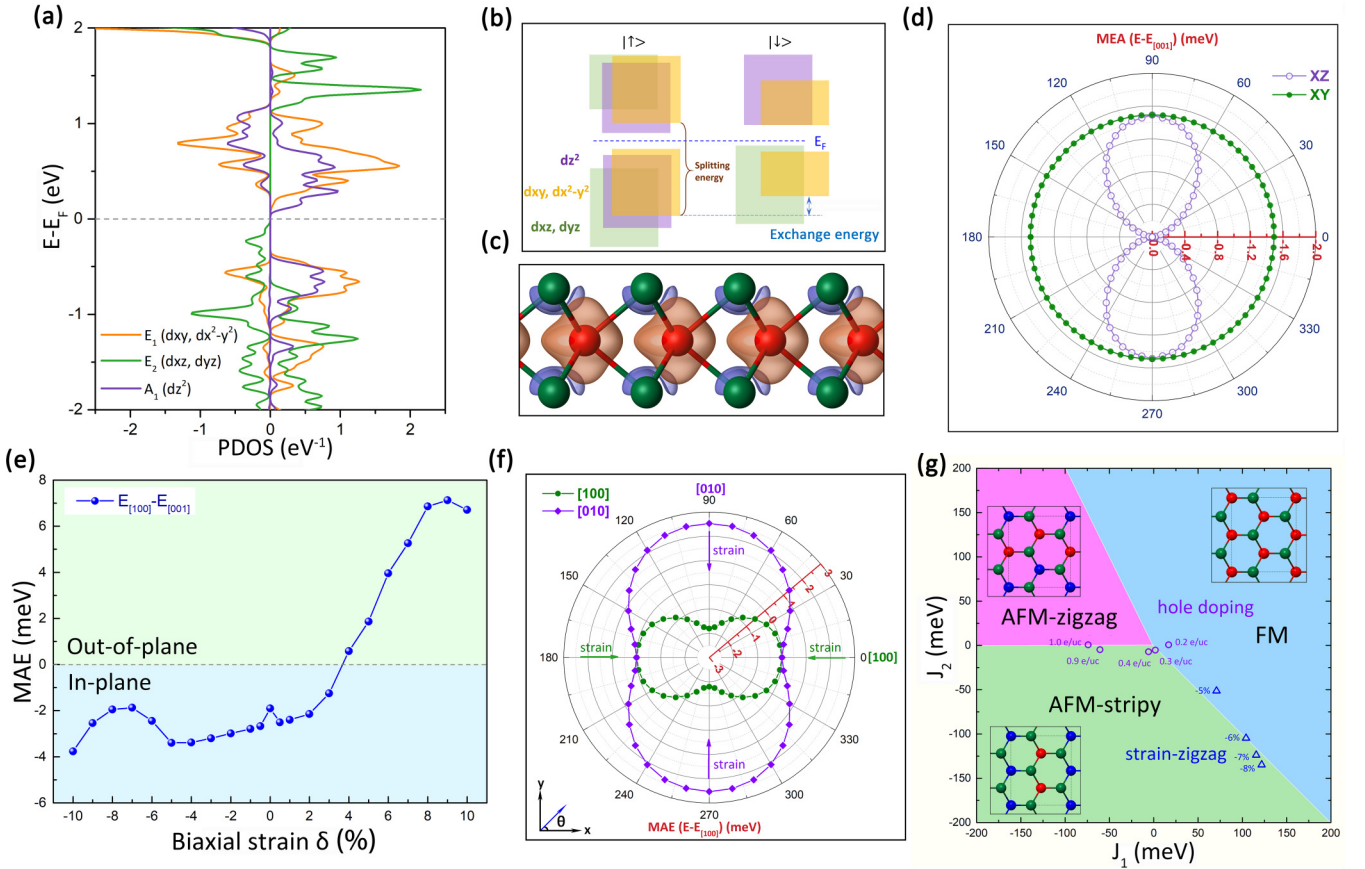
FIG. 3. (a) PDOS and (b) the schematic energy level of H-VTe$_2$. (c) Net spin-density distribution of H-VTe$_2$. (d) The MAE as a function of magnetization direction in XY (XZ) plane and (e) biaxial strain. (f) Effects of external in-plane uniaxial strain on the MAE. The energy of the configuration with magnetic moment pointing to [100] is set as 0 eV. (g) The magnetic phase diagram and corresponding magnetic orders with different exchange coefficients J_1 and J_2.

Heisenberg model is used:

$$H_{ex} = E_0 - \sum_{\langle i,j \rangle} J_1(\boldsymbol{S}_i \cdot \boldsymbol{S}_j) - \sum_{\langle i,j' \rangle} J_2(\boldsymbol{S}_i \cdot \boldsymbol{S}_{j'}), \quad (4)$$

where E_0 is the energy of the ground state without spin-polarized configuration, J_{ij} represents the isotropic exchange interaction between the ith and jth sites, and the first- (J_1) and the second (J_2)-nearest neighbor exchange interactions between V atoms are taken into consideration during calculations [68].

To get the exact value of the J_1 and J_2, three kinds of magnetic orders, i.e., the ferromagnetism (FM), stripy antiferromagnetism (AFM-stripy), and zigzag antiferromagnetism (AFM-zigzag) are considered. (Fig. S15). The in-plane spin S_x is used due to the isotropic IP MCA, and the exchange equations can be expressed as

$$E_{FM} = E_0 - 6J_1 S_x^2 - 6J_2 S_x^2, \quad (5a)$$

$$E_{AFM-stripy} = E_0 + 2J_1 S_x^2 + 2J_2 S_x^2, \quad (5b)$$

$$E_{AFM-zigzag} = E_0 + 2J_1 S_x^2 - 2J_2 S_x^2. \quad (5c)$$

The calculated exchange coefficients J_1 and J_2 are listed in Table II, and the H-VTe$_2$ has the ferromagnetic ground state.

Based on the mean-field approximation [69],

$$T_C = \frac{2}{3k_B} S^2 (n_1 J_1 + n_2 J_2), \quad (6)$$

where n_1 and n_2 the nearest-neighbor (NN) and the second-nearest neighbor (second NN) magnetic coordinates, respectively, k_B is the Boltzmann constant. The estimated Curie temperature T_C is around 317 K, which is consistent with the Tc value of 325 K obtained from the Monte Carlo simulation based on the Heisenberg model with both J_1 and J_2 as shown in Fig. S16.

By adjusting the ratio of J_1 and J_2, it is possible to modulate the magnetic ground state. Figure 3(g) shows the magnetic phase diagram of H-VTe$_2$ as a function of the J_1 and J_2, since J_1 is determined by the competition of direct exchange and superexchange interaction. The direct exchange originates from

TABLE II. Calculated parameters of spin Hamiltonian. (The V in the table refers to vanadium atom.)

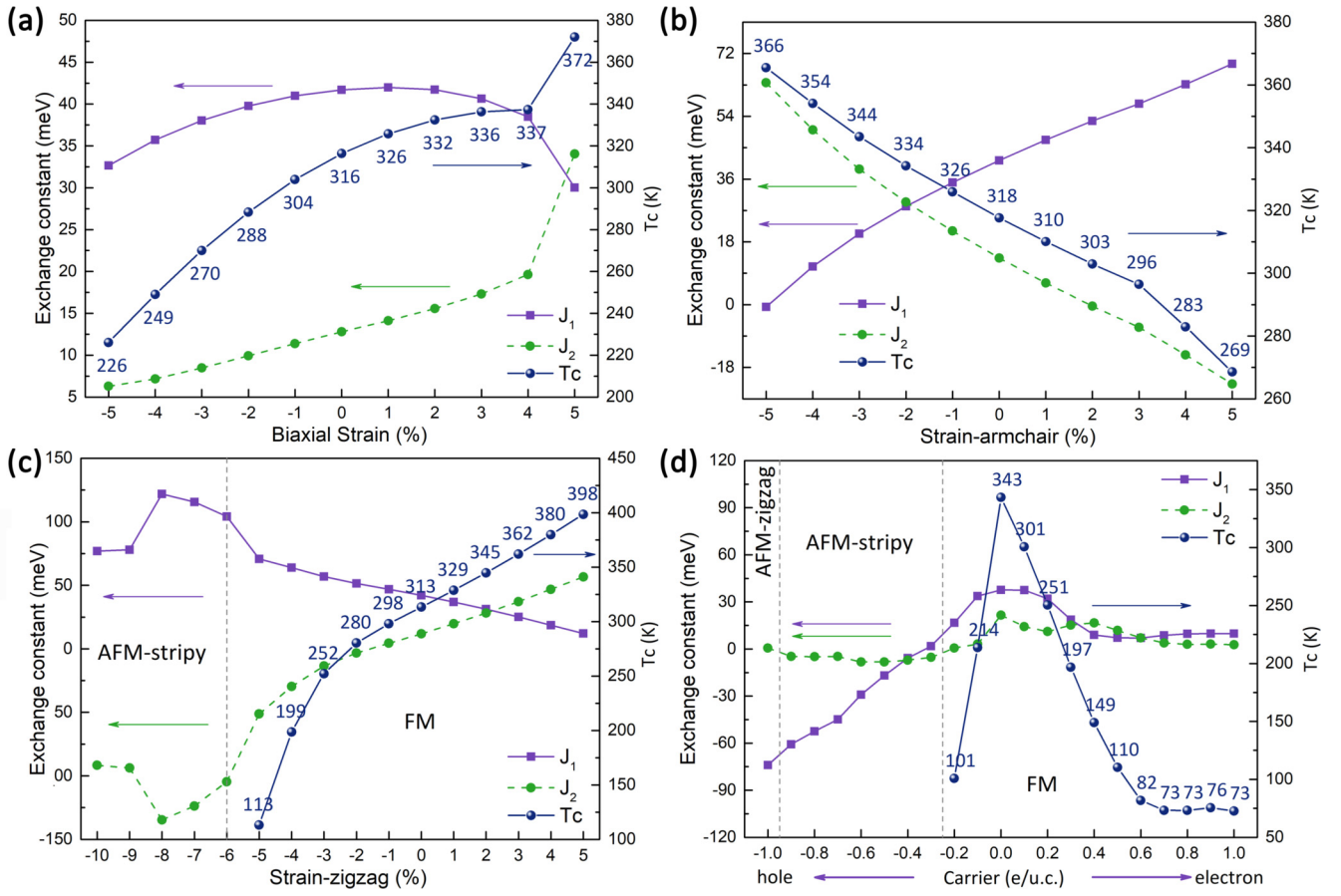| FM (meV/V)	AFM-stripy (meV/V)	AFM-zigzag (meV/V)	J_1 (meV/V)	J_2 (meV/V)	Azz (meV/V)
0.000	107.968	96.190	5.276	1.472	−5.986

FIG. 4. The effects of (a) biaxial strain, (b) armchair uniaxial strain, (c) zigzag uniaxial strain, and (d) carrier on the value of magnetic exchange constant J_1 and J_2 and ferromagnetic Curie temperature Tc.

the $3d^1$ electron hopping between the nearest V^{4+} and tends to form AFM order due to Pauli's principle. The superexchange interaction involves the hopping between magnetic V and nonmagnetic Te atoms, and it tends to be FM order in H-VTe$_2$ according to the Goodenough-Kanamori-Anderson rules with the V-Te-V angle close to $90°$ [70,71]. The partially occupied d states with $3d^1$ low-spin states for V^{4+} weaken direct inter-action [72] and the strong V–Te bonding (Fig. S8) enhances the superexchange interaction, so the J_1 is positive for FM exchange in H-VTe$_2$. For the second-NN interaction J_2, the direct exchange can be ignored and the super-superexchange effect [73] with electrons hopping through several Te atoms [Fig. S17(b)] is dominant. As shown in Fig. S18, the angles of V-Te $\cdots$ Te have values of $131.551°$ and $90°$, and the nearest distance of Te-Te in H-VTe$_2$ is 3.626 Å, leading to the FM coupling according to the super-superexchange picture [Fig. S17(c)].

C. Strain engineering the magnetic and transport properties of H-VTe$_2$.

Strain engineering is widely used in the semiconductor industry; since the Te-Te distance and V-Te $\cdots$ Te angles will change under the external strains [74,75], we explore the strain tunability of the J_1 and J_2 and magnetic Curie temperature [76]. As shown in Fig. 4, the strain can be an effective way to modulate the magnetic properties of H-VTe$_2$.

It is found that the 6% compressive uniaxial strain along the zigzag direction induces the FM to AFM-stripy phase transition. The compressive strains shorten the distance of V-V and reduce the angle in both V-Te-V and V-Te $\cdots$ Te, weakening FM exchange interaction in J_1 and J_2. We noted that the point group of H-VTe$_2$ will change from original D_{3h} to C_{2v} under uniaxial strain, the first-NN and second-NN V atoms for V_1 shown in Fig. S19 will be divided into two groups of inequivalent atoms, i.e., V_2 and V_3 for the NN and V_4 and V_5 for the second-NN V atoms, respectively. They have different influences on exchange parameters J_1 and J_2 and the phase transition (Table SIV). The Curie temperature T_C can be predicted based on the mean-field approximation in Eq. (6). The calculated results are shown in Fig. 4, where the trend of T_C is consistent with J_2 since J_2 is more intensive to the external strain.

On the other hand, carrier dopings can also be used to tune the phase transition. The hole dopings reduce the electron hybridization between Te-Te and V-Te and make the FM to AFM phase transition favorable, as shown in Fig. 4(d), while for electron doping, the V-V interaction is enhanced as the electrons are mainly doped in the d orbitals of V atoms, favoring the FM states. Carrier doping is believed to be a general technique to modulate the phase transition of the TMD materials [77,78]. In summary, the overall effects of strain and carrier doping are shown in triangle and circle symbols in Fig. 3(g).
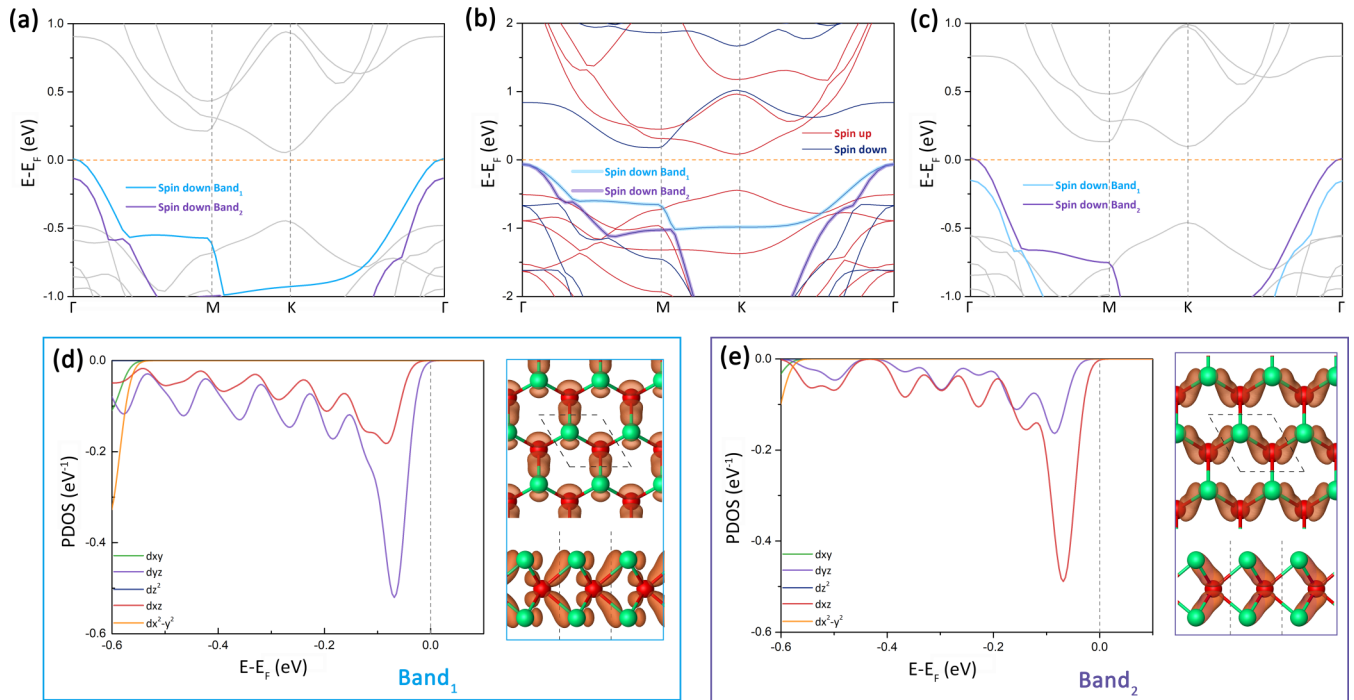
FIG. 5. Semiconductor-semimetal transition under the uniaxial strain along [100] direction. The band structure under (a) 2% tensile strain, (b) no strain, and (c) 2% compressive strain. The PDOS and real-space wave function of (d) band$_1$ and (e) band$_2$ shown in Fig. 4(b).

The strains cannot only determine the magnetic ground state of H-VTe$_2$, but also greatly affect its transport properties. As shown in Figs. 5(a) and 5(c), under 2% in-plane compressive and tensile strains, there is a semiconductor to semimetal phase transition in H-VTe$_2$. Two of the spin-down bands near valence-band maximum (VBM), denoted as band$_1$ and band$_2$, are degenerate at the Γ point in the nonstrain state. As shown in Figs. 5(d) and 5(e), the real-space wave functions of band$_1$ and band$_2$ have strong anisotropic, leading to their nondegeneracy at the Γ point under in-plane uniaxial strains. Particularly, the d_{xz} orbital of band$_2$ moves upward and crosses the E_F due to the shortened bonding length when the uniaxial compressive strain is larger than 2%. Similarly, the d_{yz} orbital of band$_2$ goes across the E_F under 2% uniaxial tensile strain, leading to the semimetal transition. All these suggest great potential for H-VTe$_2$ in the application of spintronic electronics, e.g., generating and detecting spin currents. Previous works have proposed to observe the quantum anomalous Hall effect in an in-plane magnetic system, so the ferromagnetic H-VTe$_2$ semiconductor provides a suitable platform to test these quantum effects [79].

Based on the above strain-dependent magnetic and electronic properties, a simplified schematic device is proposed in Fig. 6 to utilize the semiconductor-semimetal phase transition of H-VTe$_2$ under uniaxial strain. The strain-induced semiconductor to semimetal phase transition greatly changes the conductivity of H-VTe$_2$ [80], and a large resistance ratio is expected. A tunneling magnetoresistive (TMR) device consisting of a pinned layer (NiFe), a free layer (VTe$_2$), and a nonmagnetic layer (MgO) is constructed on top of the flexible substrate. The VTe$_2$ free layer can utilize the strain-spin coupling effect to detect the direction of the external strains. Since the band gap has a nearly linear dependence with the uniaxial compressive (tensile) strains (Fig. S20), the magnitude of the strain can also be obtained by measuring the tunneling current [16]. As shown in Fig. 6, the output voltage of the proposed TMR device reflects the strain conditions of the device, so it can be used as a detector to sense both the direction and magnitude of strain [81].
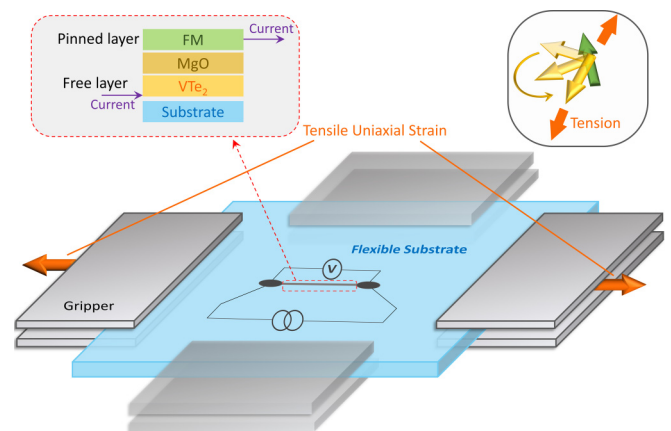

FIG. 6. Schematic illustration of TMR device that utilizes the strained induced semiconductor-metal transition. The device consists of a pinned layer, a free layer, and a nonmagnetic layer. The pinned layer is composed of a strain-insensitive in-plane ferromagnetic metal such as NiFe, and the free layer is composed of H-VTe$_2$. The inset shows the magnetic configuration under tensile strain; the yellow and green arrows represent the magnetic moment of the free layer and the pinned layer.

IV. CONCLUSION

In summary, we have systematically investigated the ground magnetic nature of VTe$_2$ and its tunability by external strain and carrier doping. It is found that the CDW phase will suppress the magnetism of T-VTe$_2$, while the semiconductor H-VTe$_2$ has a stable ferromagnetic state. However, the H-VTe$_2$ has higher formation energy compared with the T-VTe$_2$ and the CDW phase. We proposed that carrier doping or atom doping could be a feasible way to achieve the H-VTe$_2$ ground state in the experiment. Interestingly, the magnetocrystalline anisotropy and the magnetic ground state of H-VTe$_2$ can be modulated by external strain fields. A tensile biaxial strain of 4% can shift the easy-magnetization axis from in plane to out of plane, leading to the out-of-plane magnetism. Furthermore, the uniaxial strain can also modulate the direction of in-plane magnetism due to the strain-spin coupling. The compressive uniaxial strain and hole doping can also change the H-VTe$_2$ magnetic ground state from FM to AFM. Finally, a phase transition from semiconductor to semimetal is discovered under a 2% uniaxial strain. These singular and abundant physical capabilities make the H-VTe$_2$ a good candidate in 2D spintronics, sensing, and logical devices.

[1] Q. H. Wang, K. Kalantar-Zadeh, A. Kis, J. N. Coleman, and M. S. Strano, Electronics and optoelectronics of two-dimensional transition metal dichalocogenides, Nat. Nanotechnol. **7**, 699 (2012).

[2] S. Manzeli, D. Ovchinnikov, D. Pasquier, O. V. Yazyev, and A. Kis, 2D transition metal dichalcogenides, Nat. Rev. Mater. **2**, 17033 (2017).

[3] J. Li, B. Zhao, P. Chen, R. X. Wu, B. Li, Q. L. Xia, G. H. Guo, J. Luo, K. Zang, Z. W. Zhang, H. F. Ma, G. Z. Sun, X. D. Duan, and X. F. Duan, Synthesis of ultrathin metallic MTe$_2$ (M = V, Nb, Ta) single-crystalline nanoplates, Adv. Mater. **30**, 1801043 (2018).

[4] C. S. Lian, C. Si, and W. H. Duan, Unveiling charge-density wave, superconductivity and their competitive nature in two-dimensional NbSe$_2$, Nano Lett. **18**, 2924 (2018).

[5] H. C. P. Movva, Babak Fallahazed, K. Kim, S. Larentis, T. Taniguchi, K. Watanabe, S. K. Banerjee, and E. Tutuc, Density-dependent Quantum Hall States and Zeeman Splitting in Monolayer and Bilayer WSe$_2$, Phys. Rev. Lett. **118**, 247701 (2017).

[6] S. Kim, J. Schwenk, D. Walkup, Y. H. Zeng, F. Ghaharim, S. T. Le, M. R.Slot, J. Berwanger, S. R. Blankenship, K. Watanabe, T. Taniguchi, F. J. Ciessibl, N. B. Zhirenev, C. R. Dean, and J. A. Stroscio, Edge channels of broken-symmetry quantum Hall states in graphene visualized by atomic force microscopy, Nat. Commun. **12**, 2852 (2021).

[7] Y. J. Yu, F. Y. Yang, X. F. Lu, Y. J. Yan, Y. H. Cho, L. G. Ma, M. H. Niu, S. Kim, Y. W. Son, D. L. Feng, S. Y. Li, S. W. Cheong, X. H. Chen, and Y. B. Zhang, Gate-tunable phase transition in thin flakes of 1T-TaS$_2$, Nat. Nanotechnol. **10**, 270 (2015).

[8] M. G. Ugeda, A. J. Bradley, Y. Zheng, S. Onishi, Y. Chen, W. Ruan, C. Ojeda-Aristizabal, H. Ryu, M. T. Edmonds, H. Tsai, A. Riss, S. K. Mo, D. Lee, A. Zettl, Z. Hussain, Z. X. Shen, and M. F. Crommie, Characterization of collective ground states in single-layer NbSe$_2$, Nat. Phys. **12**, 92 (2016).

[9] J. G. Feng, D. Biswas, A. Rajan, M. D. Watson, F. Mazzola, O. J. Clark, K. Underwood, I. Markovic, M. McLaren, A. Hunter, D. M. Burn, L. B. Duffy, S. Barua, G. Balakrishnan, F. Bertran,

P. L. Fevre, T. K. Kim, G. van der Lann, T. Hesjedal, P. Wahl, and P. D. C.King, Electronic structure and enhanced charge-density wave order of monolayer VSe$_2$, Nano Lett. **18**, 4493 (2018).

[10] Y. Yi, N. O. Weiss, X. D. Duan, H. C. Cheng, Y. Huang, and X. F. Duan, van der Waals heterostructures and devices, Nat. Rev. Mater. **1**, 16042 (2016).

[11] E. C. Ahn, 2D materials for spintronic devices, 2D Mater. Appl. **4**, 17 (2020).

[12] X. H. Cai, T. C. Song, N. P. Wilson, G. Clark, M. He, X. O. Zhang, T. Taniguchi, K. Watanabe, W. Tao, D. Xiao, M. A. McGuire, D. H. Cobden, and X. D. Xu, Atomically thin CrCl$_3$: An in-plane layered antiferromagnetic insulator, Nano Lett. **19**, 3993 (2019).

[13] Z. W. Zhang, J. Z. Shang, C. Y. Jiang, A. Rasmita, W. B. Gao, and T. Yu, Direct photoluminescence probing of ferromagnetism in monolayer two-dimensional CrBr$_3$, Nano Lett. **19**, 3138 (2019).

[14] B. Huang, C. Clark, E. N. Moratella, D. R. Klein, R. Cheng, K. L. Seyler, D. Zhong, E. Schmiddgall, M. A. McGuire, D. H. Cobdan, W. Yao, D. Xiao, P. J. Herrero, and X. D. Xu, Later-dependent ferromagnetism in a van der Waals crystal down to the monolayer limit, Nature (London) **546**, 270 (2017).

[15] C. Tan, J. Lee, S. G. Jun, T. Park, S. Albarakati, J. Partridge, M. R. Field, D. G. McCulloch, L. Wang, and C. G. Lee, Hard magnetic properties in nanoflake van der Waals Fe$_3$GeTe$_2$, Nat. Commun. **9**, 1554 (2018).

[16] S. W. Jiang, L. Z. Li, Z. F. Wang, J. Shan, and K. F. Mark, Spin tunnel field-effect transistors based in two-dimensional van der Waals heterostructures, Nat. Electron. **2**, 159 (2019).

[17] T. C. Song, X. H. Cai, M. W. T. Yu, X. O. Zhang, B. Huang, N. P. Wilson, K. L. Selyer, L. Zhu, T. Taiguchi, K. Watanabe, M. A. McGuire, D. H. Cobden, D. Xiao, W. Yao, and X. D. Xu, Giant tunneling magnetoresistance in spin-filter van der Waals heterostructures, Science **360**, 1214 (2018).

[18] Z. Wang, D. D. Sapkota, T. Taniguchi, K. Watanabe, D. Mandrus, and A. F. Morpurgo, Tunneling spin valves based

in Fe$_3$GeTe$_2$/hBN/Fe$_3$GeTe$_2$ van der Waals heterostructures, Nano Lett. **18**, 4303 (2018).

[19] V. V. Kulish and W. Huang, Single-layer metal halides MX$_2$ (X = Cl, Br, I): Stability and tunable magnetism from first principles and Monte Carlo simulations, J. Mater. Chem. C **5**, 8734 (2017).

[20] L. J. Meng, Z. Zhou, M. Q. Xu, S. Q. Yang, K. P. Si, L. X. Liu, Z. G. Wang, H. N. Jiang, B. X. Li, P. X. Qin, P. Zhang, J. L. Wang, Z. Q. Liu, P. Z. Tang, Y. Ye, W. Zhou, L. H. Bao, H. J. Gao, and Y. J. Gong, Anomalous thickness dependence of Curie temperature in air-stable two-dimensional ferromagnetic 1T-CrTe$_2$ grown by chemical vapor deposition, Nat. Commun. **12**, 809 (2021).

[21] H. R. Fuh, C. R. Chang, Y. K. Wang, R. F. L. Evans, R. W. Chantrell, and H. T. Jeng, New type single-layer magnetic semiconductor in transition-metal dichalicogenides VX_2 (X = S, Se and Te), Sci. Rep. **6**, 32625 (2016).

[22] J. Du, C. Xia, W. Xiong, T. Wang, Y. Jia, and J. Li, Two-dimensional transition-metal dichalcogenides-based ferromagnetic van der Waals heterostructure, Nanoscale **9**, 17585 (2017).

[23] J. Liu, W. H. Hou, C. Cheng, H. X. Fu, J. T. Sun, and S. Meng, Intrinsic valley polarization of VSe$_2$ monolayers, J. Phys.: Condens. Matter **29**, 255501 (2017).

[24] X. L. Sui, T. Hu, J. F. Wang, B. L. Gu, W. H. Duan, and M. S. Miao, Voltage-controllable colossal magnetocrystalline anisotropy in single-layer transition metal dichalcogenides, Phys. Rev. B **96**, 041410(R) (2017).

[25] M. Esters, R. G. Hennig, and D. C. Johnson, Dynamic instabilities in strongly corrected VSe$_2$ monolayers and bilayers, Phys. Rev. B **96**, 235147 (2017).

[26] F. Arnold, R. M. Stan, S. K. Mahatha, H. E. Lund, D. Curcio, M. Dendzik, H. Bana, E. Travaglia, D. Lizzit, Z. Li, M. Bianchi, P. J. A. Miwa, M. Bremholm, P. Lizzit, P. Hofmann, and C. E. Sanders, Novel single-layer vanadium sulfide phase, 2D Mater. **5**, 45009 (2018).

[27] M. Bonilla, S. Kolekar, Y. Jiang, Y. J. Ma, H. C. Diaz, V. Kalappattil, R. Das, T. Eggers, H. R. Gutierrez, M. H. Phan, and M. Batzill, Strong room-temperature ferromagnetism in VSe$_2$ monolayers on van der Waals substrates, Nat. Nanotechnol. **13**, 289 (2018).

[28] K. Sugawara, Y. Nakata, K. Fujii, K. Nakayama, S. Souma, T. Takahashi, and T. Sato, Monolayer VTe$_2$: Incommensurate Fermi surface nesting and suppression of charge density waves, Phys. Rev. B **99**, 241404(R) (2019).

[29] Y. Umemoto, K. Sugawara, Y. Nakata, T. Takahashi, and T. Sato, Pseudogap, Fermi arc, and Peierls-insulating phase induced by 3D-2D crossover in monolayer VSe$_2$, Nano Res. **12**, 165 (2019).

[30] F. P. Zheng, Z. M. Zhou, X. Q. Qiang, and J. Feng, First-principle study of charge and magnetic ordering in monolayer NbSe$_2$, Phys. Rev. B **97**, 081101(R) (2018).

[31] Y. Wang, J. H. Ren, J. H. Li, Y. J. Wang, H. N. Peng, P. Yu, W. H. Duan, and S. Y. Zhou, Evidence of charge density wave with anisotropic gap in a monolayer VTe$_2$ film, Phys. Rev. B **100**, 241404(R) (2019).

[32] G. Y. Miao, S. W. Xue, B. Li, Z. J. Lin, X. T. Zhu, W. H. Wang, and J. D. Guo, Real-space investigation of the charge density wave in VTe$_2$ monolayer with broken rotational and mirror symmetries, Phys. Rev. B **101**, 035407 (2020).

[33] P. E. Blöchl, Projector augmented-wave method, Phys. Rev. B **50**, 17953 (1994).

[34] G. Kresse and D. Joubert, From ultrasoft pseudopotentials to the projector augmented-wave method, Phys. Rev. B **59**, 1758 (1999).

[35] J. P. Perdew, K. Burke, and M. Ernzerhof, Generalized Gradient Approximation Made Simple, Phys. Rev. Lett. **77**, 3865 (1996).

[36] A. V. Krukau, O. A. Vydrov, A. F. lzmaylov, and G. E. Scuseria, Influence of the exchange screening parameter on the performance of screened hybrid functionals, J. Chem. Phys. **125**, 224106 (2006).

[37] D. Hobbs, G. Kresse, and J. Hafner, Fully unconstrained noncollinear magnetism within the projector augmented-wave method, Phys. Rev. B **62**, 11556 (2000).

[38] Y. C. Wang, J. Lv, L. Zhu, and Y. M. Ma, CALYPSO: A method for crystal structure prediction, Comput. Phys. Commun. **183**, 2063 (2012).

[39] A. I. Liechtenstein, V. I. Anisimov, and J. Zanne, Density-functional theory and strong interactions: Orbital ordering in Mott-Hubbard insulators, Phys. Rev. B **52**, R5467 (1995).

[40] F. Aryasetiawan, M. Imada, A. George, G. Kotliar, S. Biermann, and A. I. Lichtenstein, Frequency-dependent local interactions and low-energy effective models from electronic structure calculations, Phys. Rev. B **70**, 195104 (2004).

[41] S. Nosé, A unified formulation of the constant temperature molecular dynamics methods, J. Chem. Phys. **81**, 511 (1984).

[42] H. C. Andersen, Molecular dynamics simulations at constant pressure and/or temperature, J. Chem. Phys. **72**, 2384 (1980).

[43] A. Togo and I. Tanaka, First principles phonon calculations in materials science, Scr. Mater. **108**, 1 (2015).

[44] See Supplemental Material at http://link.aps.org/supplemental/10.1103/PhysRevB.105.214403 for the possible phases of VTe$_2$, possible configurations of CDW-phase VTe$_2$, detailed electronic properties of H-VTe$_2$, temperature evolution of magnetic properties, and scheme diagrams for exchange interaction within H-VTe$_2$.

[45] T. Dai, S. D. Kang, X. Y. Ma, S. Dang, H. W. Li, Z. L. Ruan, W. Q. Zhou, P. Hu, S. W. Li, and S. X. Wu, Multiple transitions of charge density wave order in epitaxial few-layered 1T'-VTe$_2$ films, J. Phys. Chem. C **123**, 18711 (2019).

[46] H. T. Liu, Y. Z. Xue, J. A. Shi, R. A. Guzman, P. P. Zhang, Z. Zhou, Y. G. He, C. Bia, L. M. Wu, R. S. Ma, J. C. Chen, J. H. Yao, H. T. Yang, C. M. Shen, W. Zhou, L. H. Bao, and H. J. Gao, Observation of the Kondo effect in multilayer single-crystalline VTe$_2$ nanoplates, Nano Lett. **19**, 8572 (2019).

[47] P. K. J. Wong, W. Zhang, J. Zhou, F. Bussolotti, X. M. Yin, L. Zhang, A. T. N'Diaye, S. A. Morton, W. Chen, J. Goh, M. P. de Jong, Y. P. Feng, and A. T. S. Wee, Metallic 1T phase, 3d^1 electronic configuration and charge wave order in molecular beam epitaxy grown monolayer vanadium ditelluride, ACS Nano **13**, 12894 (2019).

[48] E. C. Stoner, Collective electron specific heat and spin paramagnetism in metals, Proc. R. Soc. Lond. A **154**, 656 (1936).

[49] H. L. Zhuang, P. R. C. Kent, and R. G. Hennig, Strong anisotropy and magnetostriction in the two-dimensional Stoner ferromagnet Fe$_3$GeTe$_2$, Phys. Rev. B **93**, 134407 (2016).

[50] R. S. Li, Q. Shao, E. Gao, and Z. Liu, Elastic anisotropy measure of two-dimensional crystal, Extreme Mech. Lett. **34**, 100615 (2020).

[51] J. D. Lin, C. Han, F. Wang, R. Wang, D. Xiang, S. Q. Qin, X. A. Zhang, L. Wang, H. Zhang, A. T. S. Wee, and W. Chen, Electron-doping-enhanced trion formation in monolayer molybdenum disulfide functionalized with cesium carbonate, ACS Nano **8**, 5323 (2014).

[52] C. E. Sanders, M. Dendzik, A. S. Ngankeu, A. Eich, A. Bruix, M. Bianchi, J. A. Miwa, B. Hammer, A. A. Khajetoorians, and P. Hofmann, Crystalline and electronic structure of single-layer TaS$_2$, Phys. Rev. B **94**, 081404(R) (2016).

[53] Z. Muhammad, K. J. Mu, H. F. Mu, H. F. Lv, C. Q. Wu, Z. U. Rehman, M. Habib, Z. Sum, X. J.Wu, and L. Song, Electron doping induced semiconductor to metal transition in ZrSe$_2$ layers via copper atomic intercalation, Nano Res. **11**, 4914 (2020).

[54] M. Beaulame, T. Breard, G. Guelou, A. V. Powell, P. Vaqueiro, and E. Guilmeau, Electron doping and phonon scattering in Ta$_{1+x}$S$_2$ thermoelectric compounds, Acta Mater. **78**, 86 (2014).

[55] Y. Saito and Y. Iwasa, Amibipolar insulator-to-metal transition in black phosphorus by ionic liquid gating, ACS Nano **9**, 3192 (2015).

[56] F. Joucken, Y. Tison, P. L. Fevre, A. Tejeda, A. Taleb-Ibeahimi, E. Conrad, V. Repain, C. Chacon, Amandine Bellec, Y. Girard, S. Rousset, J. Ghijsen, R. Sporken, H. Amara, F. Ducastelle, and J. Lagoute, Charge transfer and electronic doping in nitrogen-doped graphene, Sci. Rep. **5**, 14564 (2015).

[57] A. D. Becke and K. E. Edgecombe, A simple measure of electron localization in atomic and molecular systems, J. Chem. Phys. **92**, 5397 (1990).

[58] A. Savin, R. Nesper, S. Wengert, and T. F. Fassler, ELF: The electron localization function, Angew. Chem. **36**, 1808 (1997).

[59] C. Zhu, B. Lei, F. Meng, J. Cui, W. Zhuo, W. Wang, Z. Xiang, and X. Chen, Realising ferromagnetism in a field-effect transistor based on VSe$_2$ thin flakes, Adv. Electron. Mater. 2101383 (2022).

[60] G. Henkelman and H. Jonsson, A climbing image nudged elastic band method for finding saddle points and minimum energy paths, J. Chem. Phys. **113**, 9901 (2000).

[61] D. Voiry, H. Yamaguchi, J. Li, R. Silva, D. C. B. Alves, F. Fujita, M. Chen, T. Asefa, V. B. Shenoy, G. Eda, and M. Chhowalla, Enhanced catalytic activity in strained chemically exfoliated WS$_2$ nanosheets for hydrogen evolution, Nat. Mater. **12**, 850 (2013).

[62] Y. Hu, X. Y. Liu, Z. H. Shen, Z. F. Luo, Z. G. Chen, and X. L. Fan, High Curie temperature and carrier mobility of novel Fe, Co and Ni carbide MXenes, Nanoscale **12**, 11627 (2020).

[63] P. Bruno, Tight-binding approach to the orbital magnetic moment and magnetocrystalline anisotropy of transition-metal monolayer, Phys. Rev. B **39**, 865 (1989).

[64] A. P. Chen and Y. P. Feng, Modulation multiferroic control of magnetocrystalline anisotropy using 5d transition metal capping layers, ACS Appl. Mater. Interfaces **12**, 25383 (2020).

[65] A. B. Shick, Coulomb correlations and magnetic anisotropy in ordered $L1_0$CoPt and FePt alloys, Phys. Rev. B **67**, 172407 (2003).

[66] P. Blonski and J. Hafner, Magnetic anisotropy of transition-metal dimers: Density functional calculations, Phys. Rev. B **79**, 224418 (2009).

[67] C. Gong, E. M. Kim, Y. Wang, G. Lee, and X. Zhang, Multiferroicity in atomic van der Waals heterostructures, Nat. Commun. **10**, 2657 (2019).

[68] H. Yang, A. Thiaville, S. Robert, A. Fert, and M. Chshiev, Anatomy of Dzyaloshinskii-Moriya Interaction at Co/Pt Interfaces, Phys. Rev. Lett. **115**, 267210 (2015).

[69] X. Lu, R. Fei, and L. Yang, Curie temperature of emerging two-dimensional magnetic structures, Phys. Rev. B **100**, 205409 (2019).

[70] J. B. Goodenough, Theory of the role of covalence in the perovskite-type manganites [La, M(II)]MnO$_3$, Phys. Rev. **100**, 564 (1955).

[71] J. B. Goodenough, An interpretation of the magnetic properties of the perovskite-type mixed crystal La$_{1-x}$Sr$_x$CoO$_{3-\lambda}$, J. Phys. Chem. Solids **6**, 287 (1958).

[72] A. Ushakov, D. Kukusta, A. Yaresko, and D. Khomskii, Magnetism of layered chromium sulfides MCrS$_2$ (M = Li, Na, K, Ag, and Au): A first-principles study, Phys. Rev. B **87**, 014418 (2013).

[73] N. Sivadas, M. W. Daniels, R. H. Swendsen, S. Okamoto, and D. Xiao, Magnetic ground state of semiconducting transition-metal trichalcogenide monolayer, Phys. Rev. B **91**, 235425 (2015).

[74] W. Yao, S. Wang, Y. Lu, J. Jiang, and S. A. Yang, Strain-induced isostructural and magnetic phase transition in monolayer MoN$_2$, Nano Lett. **16**, 4576 (2016).

[75] C. Hua, H. Bai, Y. Zheng, S. Xu, S. A. Yang, Y. Lu, and S. Wei, Strong coupled magnetic and electric ordering in monolayer of metal thio(seleno)phosphates, Chin. Phys. Lett. **38**, 077501 (2021).

[76] M. H. Whangbo, H. J. Koo, and D. Dai, Spin exchange interactions and magnetic structures of extended magnetic solids with localized spins: Theoretical descriptions on formal, quantitative and qualitative levels, J. Solid State Chem. **176**, 417 (2003).

[77] X. Xi, H. Berger, L. Ferró, J. Shan, and K. F. Mak, Gate Tuning of Electronic Phase Transitions in Two-Dimensional NbSe$_2$, Phys. Rev. Lett. **117**, 106801 (2016).

[78] Y. Wang, J. Xiao, H. Zhu, Y. Li, Y. Alsaid, K. Y. Fong, Y. Zhou, S. Wang, W. Shi, Y. Wang, A. Zettl, E. J. Reed, and X. Zhang, Structural phase transition in monolayer MoTe$_2$ driven by electrostatic doping, Nature (London) **550**, 487 (2017).

[79] Z. Liu, G. Zhao, B. Liu, Z. F. Wang, J. L. Yang, and F. Liu, Intrinsic Quantum Anomalous Hall Effect with In-Plane Magnetization: Searching Rule and Material Prediction, Phys. Rev. Lett. **121**, 246401 (2018).

[80] Z. F. Wu, Y. Huan, R. Huang, X. L. Chen, Y. Q. Guo, Y. H. He, W. Li, Y. Cai, and N. Wang, Semimetallic-to-metallic transition and mobility enhancement enabled by reversible iodine doping of graphene, Nanoscale **6**, 13196 (2014).

[81] S. Ota, A. Ando, and D. Chiba, A flexible giant magnetoresistive device for sensing strain direction, Nat. Electron. **1**, 124 (2018).